Digital-signal-processor-based dynamic imaging system for optical tomography

Joseph M. Lasker, James M. Masciotti, and Matthew Schoenecker
Department of Biomedical Engineering, Columbia University, 500 West 120th Street, 351 Engineering Terrace MC8904, New York, New York 10027

Christoph H. Schmitz
Department of Neurology, Charité University Medicine, Charitéplaz 1, 10117 Berlin, Germany

Andreas H. Hielscher
Department of Biomedical Engineering, Columbia University, 500 West 120th Street, 351 Engineering Terrace MC8904, New York, New York 10027 and Department of Radiology, Columbia University, 630 West 168th Street, MC28, New York, New York 10032

(Received 2 May 2007; accepted 18 July 2007; published online 31 August 2007)

In this article, we introduce a dynamic optical tomography system that is, unlike currently available analog instrumentation, based on digital data acquisition and filtering techniques. At the core of this continuous wave instrument is a digital signal processor (DSP) that collects, collates, processes, and filters the digitized data set. The processor is also responsible for managing system timing and the imaging routines which can acquire real-time data at rates as high as 150 Hz. Many of the synchronously timed processes are controlled by a complex programable logic device that is also used in conjunction with the DSP to orchestrate data flow. The operation of the system is implemented through a comprehensive graphical user interface designed with LABVIEW software which integrates automated calibration, data acquisition, data organization, and signal postprocessing. Performance analysis demonstrates very low system noise (~1 pW rms noise equivalent power), excellent signal precision (<0.04%–0.2%) and long term system stability (<1% over 40 min). A large dynamic range (~190 dB) accommodates a wide scope of measurement geometries and tissue types. First experiments on tissue phantoms show that dynamic behavior is accurately captured and spatial location can be correctly tracked using this system. © *2007 American Institute of Physics.* [DOI: 10.1063/1.2769577]

I. INTRODUCTION

A. Optical tomography

Over the last ten years considerable progress has been made towards a novel biomedical imaging modality often referred to as diffuse optical tomography (DOT).[1–5] This modality is based on delivering low energy electromagnetic radiation in the near-infrared wavelength range ($700\ \text{nm} < \lambda < 900\ \text{nm}$) to one or more locations on the surface of the tissue under investigation and measuring transmitted and backscattered intensities through tissue depths up to ~10 cm. The propagation of light in biomedical tissue is governed by the spatially varying scattering and absorption properties of the medium, which are described in the framework of scattering and absorption coefficients, μ_s and μ_a, given in units of 1/cm. Also commonly used is the reduced or transport scattering coefficient $\mu_s' = (1-g)\mu_s$, where $g \in [-1,1]$ is a parameter that describes the anisotropic scattering properties of tissue.[6] Based on surface measurements of transmitted and reflected light intensities, a reconstruction is performed representing the spatial distribution of the optical properties inside the medium. From these reconstructed values computed at multiple wavelengths, distribution maps of physiologically important parameters such as oxy- and deoxyhemoglobin can be derived.

Within the field of DOT, the area of dynamic optical imaging appears particularly promising. In dynamic imaging studies, one attempts to image changes in optical properties and/or physiological parameters as they occur during a system perturbation.[7] The most prominent example may be imaging hemodynamic effects during functional or drug-induced stimulation of the brain.[8–14] The advantage of dynamic imaging over static imaging is that the images represent a change against a baseline that is defined by the system itself and this change is usually immune to static measurement errors. For example, the state of the brain changes during a stimulation (e.g., various motor tasks such as finger flexing, rat whisker stimulation, and visual stimulation) relative to its prestimulation state. These measurements allow one to calculate localized changes in parameters such as oxy-, deoxy-, or total hemoglobin, without the need for data calibration using a separate reference measurement, for example, on an intralipid tissue phantom. When capturing the functional response of vascular reactivity it should be recognized that blood pressure dynamics can have frequency components that exceed 5 Hz, and therefore fast imaging frame rates are needed to accurately capture these effects and prevent these signals from aliasing.

B. Instrumentation

Optical tomographic imaging can be performed in several different methods (for thorough reviews, see Refs. 15–17). Generally, the instrumentation can operate in one of three possible modes: time domain, frequency domain, or steady state, also known as continuous wave (CW). These approaches differ in the temporal characteristics of the illuminating source and hence their respective detection techniques. Although data imparted by time-resolved and frequency-domain methods contain a greater amount of information in the form of average propagation delay (which is related to mean pathlength), steady-state measurements offer some practical advantages[18] such as being able to achieve a large dynamic range, large signal-to-noise ratios and high temporal resolution at relatively moderate costs. The radiative sources of CW systems illuminate tissue with a constant amplitude, or are modulated by a few kilohertz, and the decay in amplitude due to target attenuation is measured.[19,20] Their relative simplicity and stable performance have made them a popular tool among researchers. Indeed, most of the presently available commercial systems operate in this mode.

1. Analog detection

One of the major drawbacks to current real-time, dynamic optical tomography systems is that the signal conditioning and data processing are performed by means of analog techniques. In early continuous wave systems, the signal amplitude at zero frequency (dc) was directly detected, perhaps nominally conditioned, but comprised no further processing.[21–24] Their simple design and relative low cost still make them an economical choice for many applications that do not require highest accuracy. However, in general these systems suffer from significant noise artifacts originating from both external (ambient light and power lines) and internal (coupling, resistive elements, amplifiers, etc.) sources. Because the optical signals being measured after traveling several centimeters through tissue can be very weak (approximately picowatts to nanowatts), this cumulative noise effect severely restricts the ability to detect explicit contributions from the optical source. This is especially true, for example, during functional activation studies of either human or animal brains or dynamic breast imaging which are all highly attenuating organs. In these cases the induced signal changes are often smaller than 1%, making it very challenging to discern the physiological signals of interest from their noisy background.

In an effort to reduce obstructive noise artifacts, some systems employ a bandwidth narrowing technique in the form of lock-in detection.[25–27] This technique is used to isolate and measure a system's response to an amplitude-modulated signal that is obscured by noise sources much larger in magnitude.[28] Lock-in or synchronous detection requires a reference signal to be generated at the carrier frequency with which the measured signal is demodulated. When multiple carrier frequencies are superimposed on one another, a system's response to each individual frequency may be similarly discriminated. As such, it has become a popular signal processing tool for measurement systems in a wide range of applications, particularly those that suffer from low signal-to-noise performance. Specifically, lock-in detection has been implemented in biomedical instrumentation to measure tissue conductivity and permittivity in electrical impedance tomography,[29] electrical impedance spectroscopy,[30,31] and optical spectrometry.[32,33]

However, even in these more advanced systems, the lock-in detection schemes and signal operations are executed in the analog domain. While this is a major improvement over direct dc measurements, these systems are still subject to numerous performance-limiting factors that are characteristic of analog phase sensitive detection (PSD) including electronic nonlinearities, signal drift, output offsets, gain error, and insufficient harmonic rejection, all of which ultimately restrict functional utility.

Physical constraints place an additional burden on the practical capabilities that may be afforded by an analog imaging system. For example, recent studies in optical tomography demonstrate increasing trends of imaging with three, four, or more different wavelengths[34–36] as additional spectral information allows investigators to formulate qualitative assessments of oxyhemoglobin and deoxyhemoglobin or quantitative valuations of additional physiologic chromophores (such as water and lipids, for example). If analog lock-in methods are used, this has a domino effect on the structural design of the data acquisition instrument, especially in systems with many parallel detectors. Every channel must provide the hardware to separate each wavelength and the means to digitize and transfer all the data to the host computer. The cost and physical size of the instrument can fast become impractical for clinical measurements, causing investigators to compromise on the number of channels that they use, the number of wavelengths, or the temporal resolution of the data acquisition.

2. Digital circuits and lock-in detection

Many of the problems associated with analog signals can be overcome by combining digital-data-acquisition and digital-signal-processing methods that are carried out through an embedded digital signal processor (DSP). In contrast to analog circuits, the operation of digital circuitry is not contingent on the precise values of the digital signals. As a result, digital circuitry is immune to most external parameters that are major contributors to analog distortion, such as temperature or aging.[37] Also, digital processing is almost completely insensitive to tolerances of component values. Consequently, benefits afforded by digital lock-in detection in their superior signal extraction capabilities and low noise performance have long been established and supported in literature.[38–41] Several publications are available describing various forms of its implementation.[42–44] In particular, the reference sine waves used for the digital lock-in detector are computed in binary format by the DSP which contains very low harmonic content and no offset. The accuracy of the multiplication (and all processing operations) is restricted to the resolution of the binary word. Using floating-point data format can increase this dynamic range further yet. As a result, the precision of the actual signal-mixing process in the digital PSD is limited only by the machine precision of the processing element. Gain error is not existent in digital

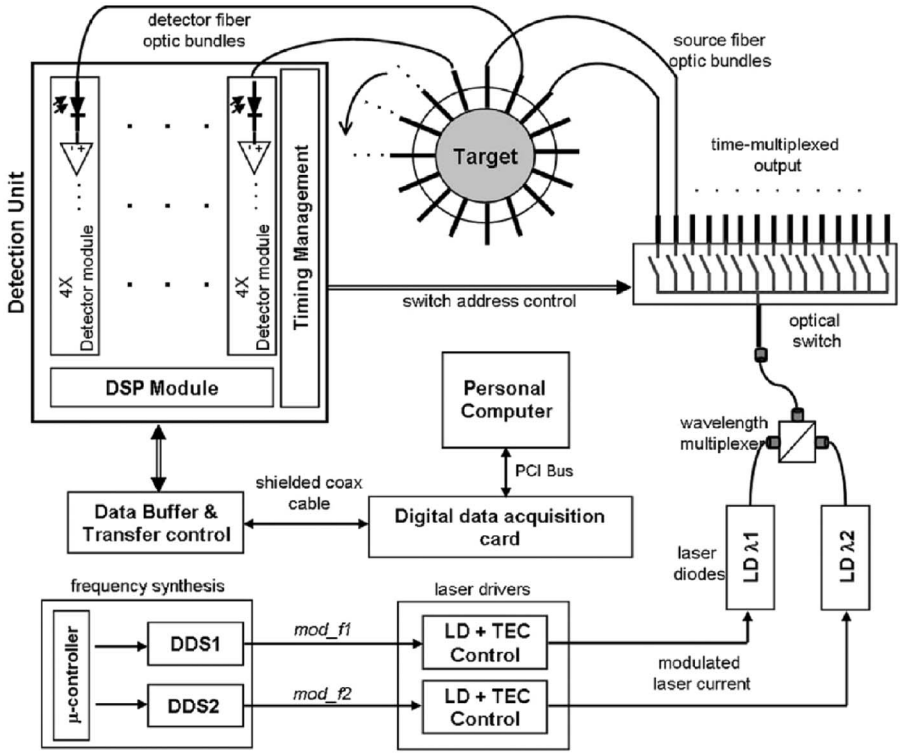

FIG. 1. Block diagram of instrument setup. DDS: direct digital synthesis. mod_f1 and mod_f2: diode modulation frequencies. LD: laser diode. TEC: thermoelectric cooler. λ_1 and λ_2: wavelengths 1 and 2. DSP: digital signal processor.

lock-in amplifiers because the amplitudes of the DSP-computed reference signals are very precise and do not fluctuate over time. Another aspect affected by the transition to the digital domain is realized in the design of the low pass filter that is typically employed during the final stage of synchronous detection. While analog filters are fast, inexpensive, and have a large dynamic range, digital filters are vastly superior in the level of performance that can be achieved.[45] Filter adjustments can by carried out by simply modifying the coefficients of the algorithm representing the filtering characteristics. These advanced filtering capabilities offer significant noise suppression in phase sensitive detection. It is primarily for these reasons that digital lock-in detection has seen increasing interest in more recent years, particularly for measuring optical attenuation[46,47] and photon counting.[48] Furthermore, the temporal response of the data acquisition is primarily determined by the settling time of the lock-in low pass filter which directly influences the dwell time of each source position. The DSP will thus promote increased imaging rates by facilitating enhanced filter operation with faster settling times.

Dedicating a DSP to perform data processing also removes large physical constraints thereby permitting the separation of many wavelengths from numerous channels in a compact, portable form without increasing system cost. In fact, such a design reduces the overall cost and physical size significantly. Moreover, due to the popularity and demand of such digital technology,[49] the processors being manufactured are continuously being improved upon in terms of speed, performance, functionality, size, power consumption, and cost.

Finally, the advantages of implementing an embedded processor are not limited to data manipulation. Given the processing power of modern DSP chips, their functionality can be expanded to include system monitoring and supervision. These chips provide an efficient means of executing dedicated tasks and organizing communication protocols with peripheral devices. Data transfer to and from the DSP are expedited efficiently through a designated input/output (I/O) processor requiring little or no overhead time. Real-time tomographic measurements involving many wavelengths can be generated, given current processor computational time on the order of $(400–600)\times10^6$ mathematic operations per second, accurate timing sequences in conjunction with a well-organized architecture, efficient data transfers, fast optical switching mechanism, and prudent filter selection. This facilitates quantifying rapid dynamic behavior of vascular and metabolic processes that occur on a subsecond time scale.

All of the above-outlined attributes encourage the design and development of a real-time, dynamic, DSP-based optical tomographic instrument. In the following we will describe in detail the design and implementation of a prototype system that makes use of the recognized benefits.

II. INSTRUMENT DESIGN

A. Overall layout

Figure 1 shows the general system layout identifying the primary building blocks involved in the imaging hardware. The design is comprised of two principal structures: one that addresses the optical illumination and light delivery to the target and another which focuses on the detection of the emerging light. Two laser diodes are coupled into one of the multiple fiber optic bundles that deliver light to the target. Each diode is driven with an ac current to produce an intensity-modulated output whose unique frequency is generated by an autonomous synthesizer. Light from the two

diodes are merged to form a single collinear beam that is focused into an optical switch. The switch redirects the light in succession to the array of fiber bundles that delivers the light to fixed locales positioned around the target. Photons exiting the tissue are coupled into separate fiber optic bundles that guide the optical signal to the multichannel detector unit. These fibers are terminated at the window of the photodiode sensor. The radiant flux produces a measurable electrical signal which is digitized and processed within the DSP through a quadrature phase sensitive lock-in detection algorithm. The resulting amplitude/s (multiple wavelengths) are transferred to a host computer via a digital data acquisition card where they are stored. Since we are digitizing many channels in parallel and have a high data throughput, a designated control module is designed to handle the system timing requirements. Instrument operation is managed through a graphical user interface, which also monitors incoming data. Each component will be described more fully in the succeeding sections with special focus on the novel digital detection technologies.

B. Light delivery

1. Illuminating source

The instrument uses continuous wave laser diodes in the near-infrared region as the radiative source. These high-powered laser diodes [HPD-1010-HHLF-TEC(FAC100,.22)FC-76505/8305—High Power Devices Inc.] operate on a narrow spectrum at 765 and 830 nm with a full width at half maximum (FWHM) of ~0.8 nm. Each diode is enclosed in a high-heat-load, fibered (HHLF) package available with a standard thermoelectric cooler (TEC) used to stabilize the laser temperature. A monitor photodiode and thermistor are mounted inside the package and provide feedback to the laser controller which regulates the power and temperature, respectively. The laser is focused into a 100 μm pigtailed fiber that hangs off of the diode and is terminated with a standard male fixed connection (FC) connector. The maximum power output of these lasers is 400 mW as measured from the distal end of the fiber. The lasers are regulated by individual laser diode controllers, model ITC110 (Thorlabs Inc.). They combine a low-noise, low-drift current source with precise temperature control.

Merging two wavelengths into a single fiber is accomplished through a wave division multiplexer (WDM) (OZ Optics Inc.) using dichroic filters. Female FC receptacles are mounted onto the WDM's housing, enabling direct coupling to the laser diode pigtailed fiber at the input ports and to the optical switch at the common port.

Demultiplexing of the irradiative beam in the time domain is a method frequently employed to separate source locations and has been adopted for our system. This is accomplished by incorporating a 1×16 multimode fiber-optics switch (Sercalo Microtechnology). Based on microelectromechanical system (MEMS) technology, this optomechanical switch can achieve very fast switching speeds with a maximum settling time specified at 5 ms. Within the optical switch, a single input is routed to a distinct output port whose location is encoded by a specific 6 bit address. The address value and switch control are managed by the timing module of the detector electronics. The output ports get coupled to the tissue interface via fiber-optic bundles.

2. Source modulation

Multiwavelength measurements may generally be obtained in one of two methods: either by serially illuminating individual monochromatic light sources or by simultaneously illuminating multiple monochromatic light sources. For our design, we seek to maximize the temporal response capabilities; therefore, all wavelengths are illuminated simultaneously.

For this reason and because a phase sensitive detection scheme is used to extract photon intensity information, the light sources are encoded with an amplitude modulating sinusoid. Being able to produce a very stable waveform at a precise frequency is imposed on us by the low pass filter that is chosen for the lock-in detection (see Sec. II C 3) and because we are not directly synchronizing the digital lock-in detection with the modulation generator. Trying to incorporate these characteristics into our light source, we note that the requisite performance and precision are not readily available from the commercial laser drivers that create their own modulating signal. As such, we opted to design custom frequency generators using a technique known as direct digital synthesis (DDS). Direct digital synthesis is a means of using digital data processing blocks to generate a frequency- and phase-tunable output signal referenced to a fixed-frequency precision clock source.[50] By integrating a high performance digital-to-analog converter (DAC) onto the DDS chip, an agile analog sinusoidal waveform can be produced. Because operations within a DDS device are primarily digital, it can offer fast switching between output frequencies, fine frequency resolution, and operation over a broad spectrum of frequencies. For our application though, we require a fixed frequency and phase output that remains stable after its initial configuration.

The direct digital synthesizer we employ is the AD9854 from Analog Devices Inc. Its circuit architect allows the generation of simultaneous in-phase (I) and quadrature (Q) signals at frequencies up to 150 MHz. Two integrated 12 bit digital-to-analog converters yield high resolution waveforms that demonstrate excellent dynamic performance. The AD9854's core provides a 48 bit frequency tuning word enabling microhertz frequency resolution.

In order to obtain even basic functionality out of the digital synthesizer, the user must program special register units which define operational parameters and regulate the digital control blocks. Therefore, incorporated into our system design is a dedicated microcontroller whose sole function is to program the DDS chips. For this purpose, the AT89S8253 microcontroller from Atmel with an 8051 architect was selected. The connections and communication between the frequency generators and the microcontroller are described in Fig. 2. A parallel data and address bus are shared by both synthesizers with individual control lines managing each one separately. In this manner, it is easy to control additional synthesizers should we wish to increase the number of wavelengths.

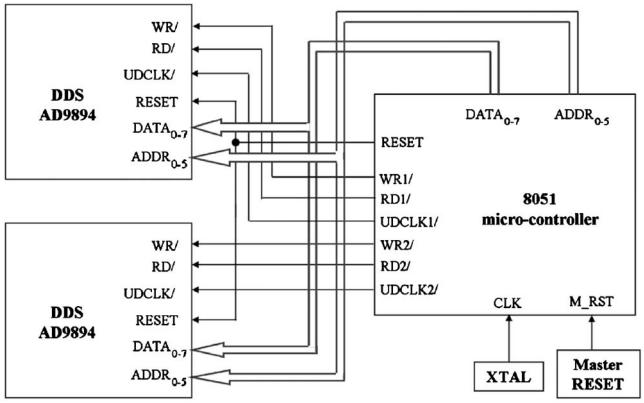

FIG. 2. Communication interface between administering microcontroller and direct digital synthesizers.

3. Signal conditioning

The processing pathway of the raw DDS output required before it is suitable to drive the laser diodes is depicted in Fig. 3. Under ordinary operation, the cosine DAC and sine DAC output an oscillating current that are 90° out of phase with each other. The 10 mA output current develops a 0.5 V peak-to-peak signal across the on-board 50 Ω *LC* filter network. To give the signal a voltage boost, an amplification stage using a slew-enhanced, voltage-feedback, operational amplifier with a gain of ~3.0 V/V is added.

Converting binary numbers $X_d[n]$ into continuous analog voltages (and vice versa) using the onboard digital-to-analog converters produce a staircase waveform as the value is approximated to the nearest quantization level. An m-bit uniform DAC has 2^m levels spaced at Δ-volt intervals. The signal to quantization noise ratio (SQNR) is defined as the ratio between the signal power P_{AV} to noise power σ_e spread out

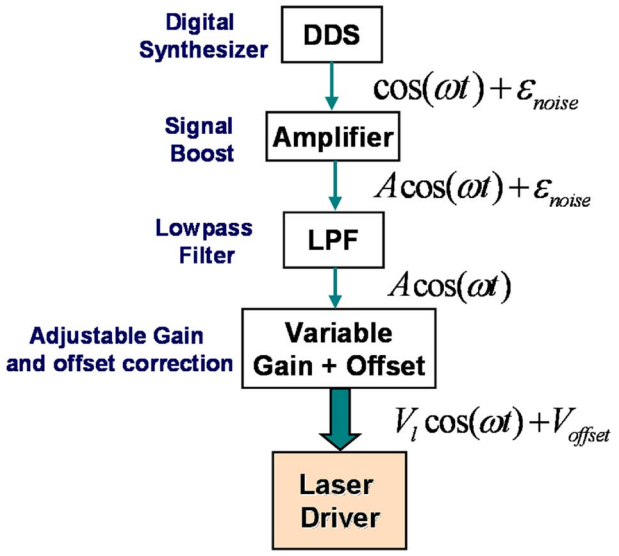

FIG. 3. Progression of signal conditioning required before synthesized waveform may drive laser diode. Steps include an initial gain of the output DAC signal followed by a bandwidth narrowing filter. The final stage consists of a variable gain and offset adjustment.

over the full bandwidth, dc to $f_s/2$. Expressed in decibels, it can be computed to be

$$\mathrm{SQNR} = 10\log_{10}\frac{[\text{Signal Power}]}{[\text{Noise Power}]}\ \mathrm{dB}$$

$$= 1.76 + 6.02m(\mathrm{dB}) + 10\log_{10}\frac{f_s}{2f_{\mathrm{BW}}}, \qquad (1)$$

where f_s is the DAC update clock and f_{BW} is the bandwidth of our signal. In order to justify using a 16 bit analog-to-digital converter (ADC) on the detector channels, we must narrow the modulation bandwidth to ensure that our signal source can at least match the precision of the detection electronics (98 dB). Otherwise, we are effectively giving up 4 bits of resolution as the precision of the final measurement is only as good as the least resolved component in the system. Therefore, the SQNR of the modulation signals must be enhanced to at least the 16 bit level.

At a maximum value of 9 kHz, our signals of interest occupy a considerably smaller bandwidth f_{BW} than the Nyquist bandwidth coming out of the DAC, providing us with a large oversampling ratio. Thus if a low pass filter is appliedto eliminate noise components outside f_{BW} then an oversampling correction factor must be included to account for the increase in SQNR (Ref. 51) as described by the last term of Eq. (1). Applying this analysis to our generated waveforms validates the need for sending them through a low pass filter. Moreover, this filter also serves to remove any images or aliased harmonics produced by the synthesizer. Therefore, after the initial gain stage, we design an eighth order Butterworth low pass, with matching performance characteristics to the antialiasing filter of the detection signal (Sec. II C 1). An identical bandwidth has also been maintained by making the cutoff frequency of 12.5 kHz. Using this quantity, we can calculate the adjusted SQNR for the narrow bandwidth signal to be just over 100 dB.

The final conditioning phase consists of a variable gain adjustment in conjunction with a variable offset correction V_{os}. Up to this point, the modulation signal swings around dc and contains zero offset. However, since the laser diode only operates when forward biased over its threshold V_{th}, i.e., at a positive current, the offset must shift the sinusoid so the voltage never falls below the threshold, $V_{\mathrm{mod}}=V_{\mathrm{os}}+A\cos(\omega t)$ where $V_{\mathrm{os}}\geqslant A+V_{\mathrm{th}}$. On-board potentiometers provide a variable gain that is used to directly adjust the output power of the laser diodes.

C. Light detection

The architecture of the signal detection circuitry is displayed in Fig. 4. Embedded in the heart of the instrument is the DSP. It is the place where the signals are collected, processed and filtered, and finally routed to the host personal computer (PC). Our instrument employs parallel detection to maximize imaging frame rate. The current design consists of 32 independent detectors, whose distribution comprises eight printed circuit boards (PCB), each accommodating four channels. A single 16-bit ADC is mounted on each board and

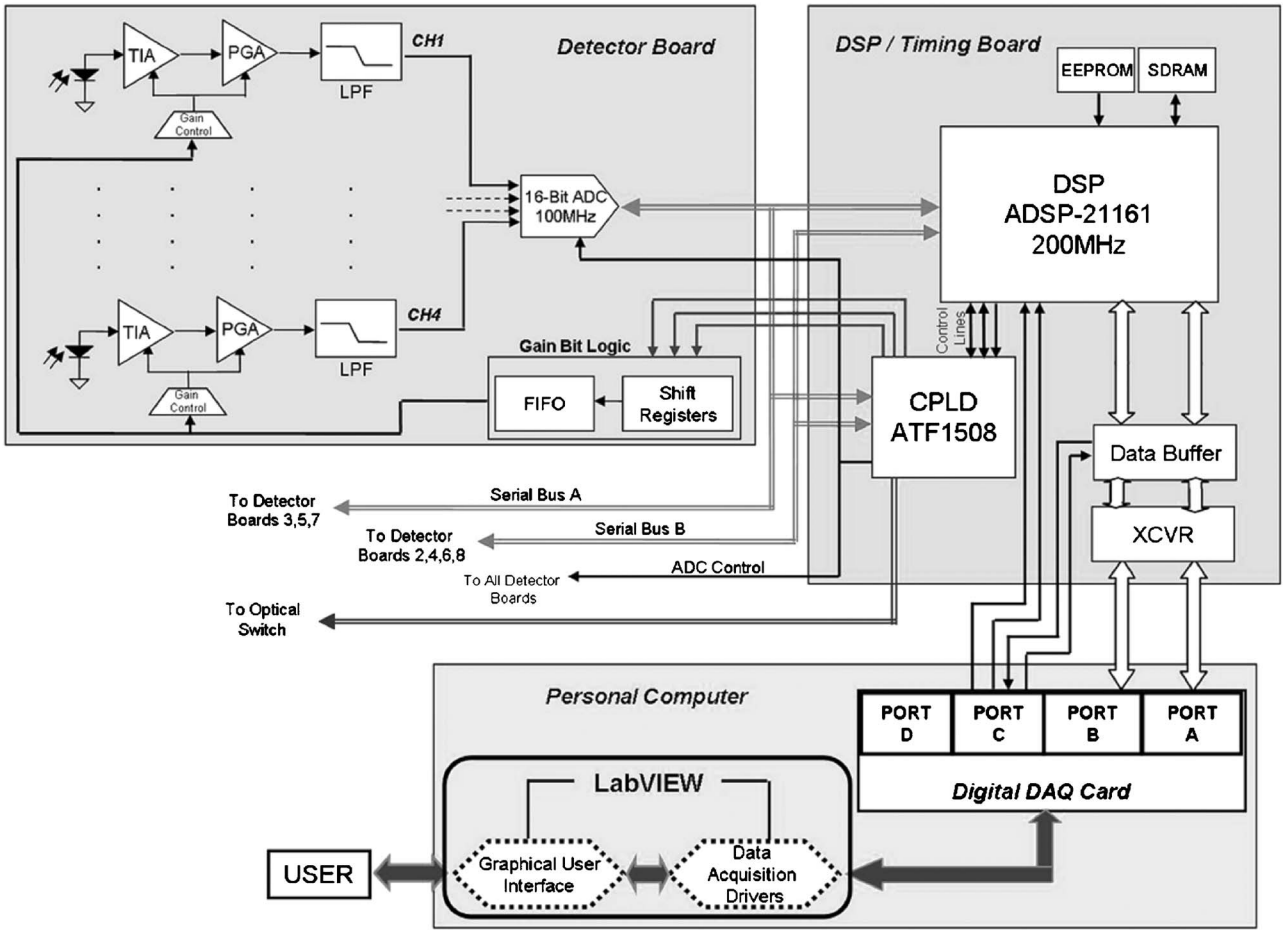

FIG. 4. Block diagram of general detection layout. Detector channels contain analog conditioning circuitry and are then sampled by the ADC. Digitized data are transferred to the DSP under precise control of the CPLD. DSP performs digital phase sensitive detection and carries out system management tasks.

accepts up to four analog input channels. Timing control consisting of the complex Programable logic device (CPLD), clock, and some support circuitry is interfaced directly with the DSP and detector boards. Electronically erasable programable read only memory (EEPROM) stores the boot-up sequence for the DSP, and external synchronous dynamic random access memory (SDRAM) are provided for temporary data storage. Additional memory buffers are used to regulate the data transfers between the fast DSP and slower host. A LABVIEW program running on the PC acts as the master controller of the instrument. We custom designed all of our boards and interconnection hardware including a DSP module that was developed for our specific relevance.

The detected analog signal must be conditioned to prepare it for digitization and further processing. Review of Fig. 4 reveals five discrete stages which comprise each detector channel and operate independently. They consist of the photodetector, transimpedance amplifier, programable gain amplifier, antialiasing low pass filter, and finally the analog-to-digital converter. In the following sections, a description of the architectural organization and motivation for their inclusion is presented in order of signal progression, originating from the sensor.

1. Analog front-end electronics

Silicon photodiodes are used as the transducer to convert photon energy to an electronic signal. They provide the sensitivity, frequency response, and linearity requisite for our application. These attributes combined with their low cost and low dark current make them optimal for our design. The photocurrent generated by the incident photons is converted to a voltage through a transimpedance amplifier (TIA). Photodiodes are sensors that exhibit very large output impedance and must therefore be designed with great care to meet the challenges of low bias current, low noise, and high gain.[52,53] For measuring over a wide range of intensities, our design allows the selection of one of three possible feedback resistor networks: 1 kΩ, 10 kΩ, or 10 MΩ. When using a very large feedback resistor such as 10 MΩ in the TIA stage, it becomes difficult to define a signal bandwidth through a capacitive network that ensures 1% passband flatness in the region of a few kilohertz (region of our modulation frequencies) due to the very low capacitance requirements. To overcome this constraint, we borrow a bandwidth extension technique introduced by Michel *et al.*[54] which compensates for the filter zero created by the feedback network. A *RC* high pass is added at the output node of the TIA whose function is to ac couple the output to the programable gain amplification (PGA) centering it around 0 V. This filter also determines the settling time of the overall analog channel as the TIA switches and comes out of momentary saturation. Our bandwidth requirements specify a high pass cutoff of 450 Hz with a corresponding settling time of 4 ms.

To further maximize the resolution of the analog-to-digital converter, extend measurement sensitivity, and increase the global dynamic range for each detector, we add an additional PGA stage. The PGA is designed to provide signal gains of 1, 10, or 100 V/V. Thus the TIA in conjunction with a subsequent programable gain amplifier offers a wide range of achievable gain scenarios ranging from 1 kV/A to 1 GV/A in steps of 10. This flexibility affords the possibility of imaging small geometries (1–3 cm)—as is common with small animals, for example—without saturating the electronics and imaging large tissue structures by bringing the highly attenuated optical signal significantly above the noise floor. Three gain bits per channel encode the individual gain settings. The intensity of light as seen at any detector channel is dependent on their relative distance from the source, tissue geometry, and tissue optical properties. As the source location changes, the received optical power observed at the stationary detectors changes concurrently. Therefore, each channel must include a high dynamic range and autonomous gain control. The corresponding bits are stored in local on-board memory for immediate access and are updated for each detection channel as the source location changes. In this way, adaptive gain control similar to the mechanism introduced by Schmitz *et al.*[25] continuously modifies the detector sensitivity, which facilitates fast source switching capabilities. By including all of the gain-bit circuitry directly onto the detection boards as opposed to having a separate timing/memory board, this design becomes more modular, making possible a straightforward expansion of detector channels.

As with any analog signal, an antialiasing filter must be applied prior to digitization to ensure that its bandwidth conforms to the Nyquist criterion.[55,56] Since our per channel sampling rate is almost ten times the band of modulation frequencies (3–9 kHz), the filter's step response can be enhanced at the expense of the frequency roll-off. Therefore, the filter chosen is an eighth order Butterworth, which affords a balance between the time-versus-frequency response trade-off. The Butterworth filter topology tends to have the flattest passband and a relatively steep roll-off. They also tend to have a fairly good time response to step inputs. With a cutoff frequency of 12.5 kHz, we achieve 0.1% attenuation at our upper limit of modulation (9 kHz). Sampling at a rate of F_s=75 ksamples/s, the Nyquist frequency becomes $\frac{1}{2}F_s$ or 37.5 kHz. Therefore, any noise appearing in the frequency range $kF_s \pm F_{\text{band}}$, for any positive integer k, where F_{band} is our 3–9 kHz detection passband, will be aliased into the passband. However, the filter attenuation at the first aliasing occurrence is approximately −117 dB and provides more than adequate noise suppression, while the amplitude of any subsequent aliasing incidences are reduced further yet. A step function at the input of the low pass filter (LPF) yields a filter settling time of 450 μs, which is not a limiting factor in the general temporal response of the detection circuitry.

Finally, the signals are digitized by an analog-to-digital converter. For our application, a successive approximation register (SAR) ADC seemed most appropriate as they afford fast sampling capabilities, reasonable precision at our modulation frequencies, and moderate power consumption. We are using the AD7655 16 bit, four-channel ADC from Analog Devices Inc. that samples at a maximum rate of 1 Msamples/s. At this frequency, each channel can easily be sampled at our target rate of 75 kHz. The serial port on the ADC is used to streamline the data into the DSP for further processing.

2. Digital electronics—DSP

From a functional standpoint, the central component of this instrument's design is a high performance digital signal processor (DSP), off of which all other elements are integrated. In particular, we are using the ADSP-21161N, which is a member of the 32 bit floating point DSP family made by Analog Devices Inc. It features Super Harvard Architecture (SHARC), and with its single-instruction-multiple-data (SIMD) computational hardware running at 100 MHz (10 ns), the processor can perform 600×10^6 mathematical operations per second. The ADSP-21161N contains one megabit of on-chip static random access memory (SRAM) that can be configured for different combinations of data and code storage. Some additional on-chip system features include a host processor interface, a dedicated I/O processor that supports 14 direct memory access (DMA) channels, four serial ports, serial peripheral interface (SPI), SDRAM controller, two link ports, external parallel bus, and glueless multiprocessing.

Because of its many functions, the ADSP-21161N takes on a multitude of responsibilities. It initiates and coordinates all system-level processes that are executed for a given task and orchestrates the transfer of measurement and gain-bit data to and from the host computer. The DSP is also responsible for uploading the gain-bit data to their respective channels and for receiving digitized samples from all 32 detectors. The timing details associated with the various functions are addressed in Sec. II D. From a processing standpoint, the DSP carries out the multifrequency, quadrature lock-in detection, which is an integral part of the system design as it plays a major role in the effective performance of the imager.

3. DSP—digital lock-in detection for multiple frequencies

One of the more compelling rationales in employing a digital processor within the system architect is its ability to efficiently perform signal processing tasks on a large quantity of data. Specifically, we demodulate the detected photons using a quadrature-based digital lock-in detection scheme to extract a target's response to individual wavelengths. The following section expounds on this technique, demonstrates how it is extended for multiple frequencies, and presents our unique exploitation of a simple low pass filter.

Our optical signal as seen by the photodiode is formed from N_m different wavelengths and may be expressed as

$$V(t) = \text{dc}_{\text{meas}} + \sum_{k=1}^{N_m} A_k \cos(2\pi f_k t + \varphi_k), \tag{2}$$

where dc_{meas} is the effective zero-frequency offset, A_k is the amplitude at wavelength k, f_k is the source (modulation) frequency, and φ_k is its respective phase shift. Typically, the

measured dc quantity of Eq. (2) contains a high level of distortion—including systematic and environmental noise—making its utility very limited. As such, this component is removed by passing the signal through a high pass filter. While an offset is later added to create a pseudobipolar signal for the ADC, it is immediately subtracted off in the DSP so it will not be included in the analysis. It follows that an ADC acquiring N_s samples every $T_s=1/f_s$ seconds, where f_s is the sampling frequency, digitizes the analog signal of channel j represented in discretized notation as

$$V_j[n]=\sum_{k=1}^{N_m} A_{j,k}\cos\left(\frac{2\pi f_k n}{f_s}+\varphi_{j,k}\right). \tag{3}$$

In order to demodulate the waveform, phase sensitive techniques require the use of reference signals. The first reference signal is the so-called "in-phase" or I reference denoted by

$$C_m[n]=P_m\cos\left(\frac{2\pi f_m n}{f_s}+\theta_m\right), \tag{4}$$

with amplitude P_m, frequency f_m, and phase shift φ_m corresponding to modulation m. Homodyne (synchronous) detection dictates that the reference frequency signal f_m must be identical to the source modulation frequency f_k. Quadrature detection is an extension of this method that removes the phase dependency from the measured value. It does this by imposing an additional reference signal per wavelength. More specifically, the quadrature reference signal $S_{\mathrm{ref}}[n]$, which is merely a 90° phase shift of the original reference $C_{\mathrm{ref}}[n]$, is defined by

$$S_m[n]=P_m\sin\left(\frac{2\pi f_m n}{f_s}+\theta_m\right). \tag{5}$$

These digitized reference signals are synthesized numerically and stored as vectors in the memory of the digital signal processor. Numerical sinusoids are naturally noise-free and calculated to an exactness that is bound only by the mathematical precision of the computation unit. Also, they need to be generated only once and then stored, which diminishes the complexity of the system. However, an expected consequence is that it does not guarantee a synchronized lock onto the source modulation hardware and may therefore exhibit a slight frequency mismatch. This is why we employ direct digital synthesis technology to generate highly stable and precise modulation frequencies.

The first step in extracting the amplitude and phase quantities of a given modulation frequency is to multiply the detected signal $V_j[n]$ with each reference $C_m[n]$ and $S_m[n]$ separately. Using the product-to-sum formulas, the product of these two discretized signals becomes a series of mixed frequency terms known as the in-phase and quadrature component, respectively,

$$I_{j,m}[n]=V_j\times C_m=\begin{cases}\dfrac{P_m A_{j,m}}{2}\left\{\cos[\varphi_{j,m}-\theta_m]+\cos\left[\dfrac{4\pi f_m n}{f_s}+(\varphi_{j,m}+\theta_m)\right]\right\}, & \text{for } k=m\\ P_m\cdot\displaystyle\sum_k\dfrac{A_{j,k}}{2}\left\{\cos\left[\dfrac{2\pi(f_k-f_m)n}{f_s}+(\varphi_{j,k}-\theta_m)\right]+\cos\left[\dfrac{2\pi(f_k+f_m)n}{f_s}+(\varphi_{j,k}+\theta_m)\right]\right\}, & \text{for } k\neq m,\end{cases} \tag{6}$$

$$Q_{j,m}[n]=V_j\times S_m=\begin{cases}\dfrac{P_m A_{j,m}}{2}\left(\sin[\varphi_{j,m}-\theta_m]+\sin\left[\dfrac{4\pi f_m n}{f_s}+(\varphi_{j,m}+\theta_m)\right]\right), & \text{for } k=m\\ P_m\cdot\displaystyle\sum_k\dfrac{A_{j,k}}{2}\left(\sin\left[\dfrac{2\pi(f_k-f_m)n}{f_s}+(\varphi_{j,k}-\theta_m)\right]+\sin\left[\dfrac{2\pi(f_k+f_m)n}{f_s}+(\varphi_{j,k}+\theta_m)\right]\right), & \text{for } k\neq m.\end{cases} \tag{7}$$

Each modulation frequency in the above equations generates two terms that get shifted along the Fourier spectrum as determined by $f_k\pm f_m$ at its respective amplitude and phase. For the special case where $f_k=f_m$, a particular modulation frequency is being synchronized with its corresponding reference, so that one component is sitting at zero frequency (dc) and the second component is positioned at twice the modulation frequency. The amplitudes of both these terms are directly proportional to the amplitudes of the detected optical signal and the reference signal and the phase difference between them. By convolving the in-phase and quadrature signals with a low pass filter whose impulse response is defined by $h_L[n]$, only the dc components are preserved while all higher frequency terms are suppressed to yield

$$X_{j,m}[n]=h_L[n]\otimes I_{j,m}[n],$$

$$X_{j,m}[n]=A_{j,m}P_m\frac{1}{2}[\cos(\varphi_{j,m}-\theta_m)], \tag{8}$$

$$Y_{j,m}[n]=h_L[n]\otimes Q_{j,m}[n],$$

$$Y_{j,m}[n]=A_{j,m}P_m\frac{1}{2}[\sin(\varphi_{j,m}-\theta_m)], \tag{9}$$

With only the two dc terms now present, the amplitude for channel j wavelength m can be calculated by taking the magnitude of the $X[n]$ and $Y[n]$ vectors,

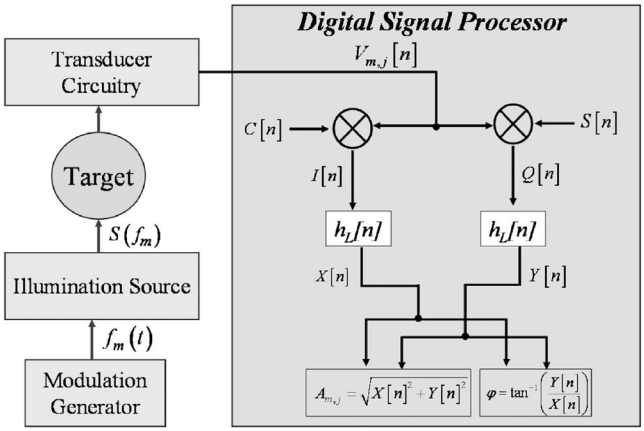

FIG. 5. Signal flow and computational sequence of extracting amplitude and phase using the quadrature digital lock-in detection method.

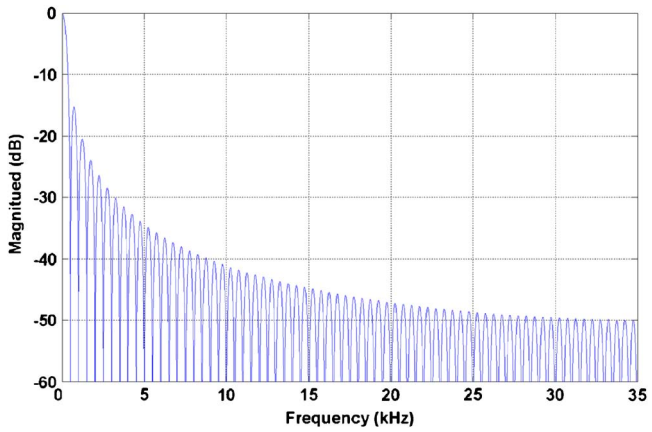

FIG. 6. (Color online) Frequency response of 150-point averaging filter sampled at 75 kHz. The frequency axis runs till Nyquist=37.5 kHz, and magnitude is calculated in decibels.

$$r_{j,m} = \sqrt{X_{j,m}^2 + Y_{j,m}^2} = \sqrt{\left(\frac{1}{2}A_{j,m}P_m\right)^2 \times [\cos^2(\phi_j) + \sin^2(\phi_j)]} = \frac{1}{2}A_{j,m}P_m, \tag{10}$$

and the phase

$$\varphi_{j,m}[n] = -\tan^{-1}\left(\frac{Y[n]}{X[n]}\right). \tag{11}$$

This method outputs a value for r that is directly related to the amplitude of channel j but independent of the phase. Figure 5 illustrates the computational progression of the quadrature lock-in detection technique that is calculated for each detector channel at every wavelength.

Designing the low pass filter for the final phase of the lock-in detection requires careful consideration as it determines the noise-rejection capabilities, data acquisition settling time, and modulation-spacing requirements. The low pass filter we have chosen to implement is an ordinary averaging filter guided by specific sampling constraints proposed by Masciotti *et al.*[57] Generally, to measure dc signals an averaging filter is optimal for removing white noise[58] and often used in instances where noise is assumed to be wideband.[59] It is shown that by judiciously choosing the sampling frequency, modulation frequencies, and the number of samples acquired, the unique frequency response of this finite impulse response (FIR) filter type can be maximally exploited.

The magnitude response of the averaging filter can be obtained as

$$|H(f)| = \left|\frac{1}{N_s}\frac{\sin(N_s\pi f/f_f)}{\sin(\pi f/f_f)}\right|. \tag{12}$$

Analysis of Eq. (12) reveals some interesting properties of this function. At $f=0$, the magnitude has a value of 1. The numerator is a sinusoid with period $2f_s/N_s$ and has zeros spaced every f_s/N_s hertz. The period of the expression is determined by the period of the denominator, which is $2f_s$. Thus, the zeros of infinite rejection can be strategically placed by appropriately selecting the sampling frequency and the number of samples averaged.[60] More specifically, the frequency response of an N_s point averaging filter sampled at frequency f_s contains zeros at multiples of f_s/N_s,

$$f_{\text{zero}} = k\frac{f_{\text{Nyquist}}}{N_s/2} = k\frac{f_s}{N_s}, \tag{13}$$

where k is any positive integer and $f_{\text{Nyquist}}=f_s/2$ is the maximum frequency represented on the spectrum. Figure 6 shows the frequency response of a 150 point averaging filter. It can be seen that all multiples of $f_s/150$ up to the Nyquist frequency have a response of zero.

To take advantage of these zero-magnitude bins, we restrict our choice of modulation frequencies to those that exhibit a zero-magnitude filter response. It is instructive to note the practical and favorable significance of adhering to the above correlations. Firstly, k complete periods are always accumulated at any particular modulation frequency. This fact can be demonstrated by the following relationships:

$$T_{\text{mod}} = T_{\text{zero}} = \frac{N_s}{k}T_s = \frac{T_{\text{acq}}}{k}, \tag{14}$$

$$\frac{T_{\text{acq}}}{T_{\text{mod}}} = k, \tag{15}$$

where $T_{\text{acq}}=N_sT_s$ is the data acquisition period for a single channel and $T_x=1/f_x$ is defined as the period of parameter x. Intuitively, this effect may be understood as a direct consequence of averaging exactly k complete periods of a sinusoidal wave form. Secondly, and more importantly, each shifted frequency component generated by the mixing stage of the lock-in fall into one of the bins resulting in the cancellation of all additive frequency components except the one being locked onto. This is in fact the principal motivation for employing the averaging filter for our application.

Following the general rule of thumb to sample no less than ten times the signal bandwidth,[61] our sampling rate of the ADC is specified to 75 kHz. Oversampling relaxes the constraints of the antialiasing filter and disperses the quantization noise over a wider bandwidth. The filter settling time can be defined as N_sT_s, which is the time it takes to collect N_s samples every T_s seconds. N_s was set at 150 samples per channel yielding a filter settling time of 2 ms to compromise

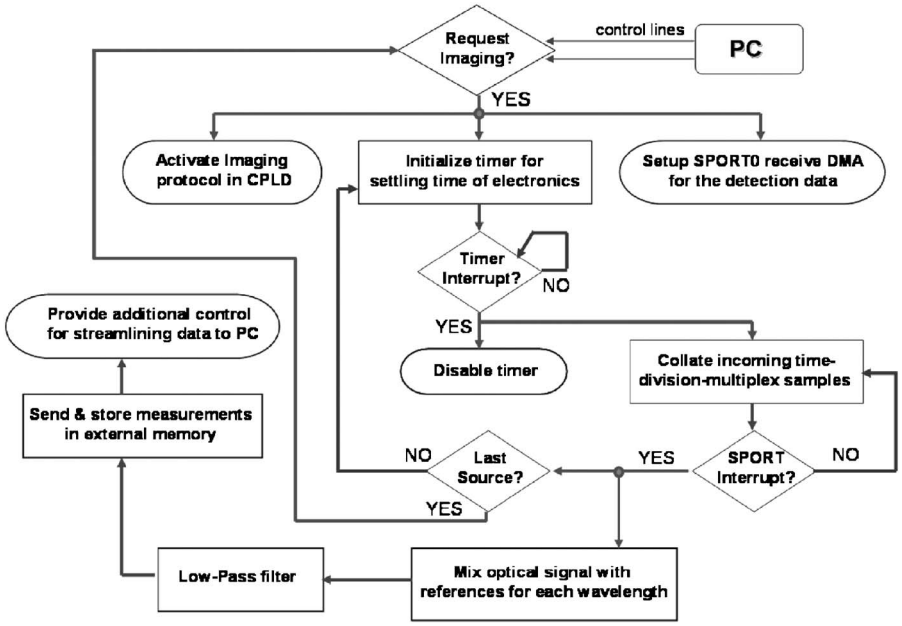

FIG. 7. Flow chart of DSP operations during an imaging cycle.

the trade-off between greater noise immunity and a shorter data acquisition period. The data acquisition period is characterized by the settling time of the analog electronics plus the settling time of the lock-in low pass filter.

D. System timing

Orchestrating the multitude of events transpiring throughout the course of an experiment presents itself as one of the major challenges to this system's design. For instance, prior to taking any measurements, optimal gain bits for each source-detector pair must be determined and downloaded to their respective memory banks. During the imaging routine, as each source position is being aligned, the gain bits must be updated for all detector channels and the settling times of both the optical switch and analog electronics must be obeyed. The sampling and data-retrieval process of all 32 detectors must be synchronized meticulously so that they can be efficiently streamlined into the DSP. Finally, after the processor has completed the lock-in detection on the data set, it must transfer the results to the host computer to be viewed, analyzed, and saved.

All instrument functions are executed through precise timing protocols between the DSP, CPLD, and a digital data acquisition card. The CPLD, as its name implies, is a high-density programable device generally based on programable array logic. A CPLD in effect acts as a multilevel state machine and can simulate a variety of standard logic operations. They are completely reconfigurable and provide a significant reduction in both cost and complexity over discrete components. While the overall functions of the imager are controlled by the DSP, the timing management of many operations is coordinated by the CPLD, as will be explained in more detail below.

1. DSP control

Upon power up, the DSP goes through a boot-up sequence that loads the programing code stored in an on-board EEPROM after which a series of system initialization procedures are followed so that internal control registers are appropriately configured for running experiments. Once the initialization is complete, the DSP drops into a low-power idle state where it waits for one of four possible instructions from the PC: acquire imaging parameters, download gain-bit values, begin imaging, or stop imaging.

Before any images may be obtained, the detection sensitivity needs to be configured for each channel individually. This is accomplished by an automated process that runs a series of "scout scans" on the experimental target and evaluates optimal settings (see Sec. II E). Three bits encode the analog amplification for each detector channel. Since the instrument can accommodate up to 32 channels, there are a total of 96 gain bits per source position. Gain-bit values for each source-detector combination are transmitted from the PC, stored in the DSP, and sequentially transmitted through the CPLD who distributes them to local memory banks. From there, they can be read out to individual detector channels at will. Section II E describes how these values are determined.

At this point, once the suitable gain bits are confirmed, the instrument is ready to begin acquiring images. During the imaging routine, the DSP operations involved are more complex as is depicted in the diagram of Fig. 7. When the DSP is instructed to acquire images, it immediately starts the 5 ms timer that is used for optical switch and analog electronics settling time and instructs the CPLD to enter the imaging state machine. During this time, the DSP configures the DMA of its serial port lines that transfer the incoming data from the ADC's. A DMA chaining routine is used to collate the time-division multiplexed samples as it enters the DSP so that they are organized by detector number in contiguous memory space. When the transfer is complete and all samples have been collected, an interrupt is triggered which initiates the lock-in detection algorithm. The calculations are cycled through for each detector channel resulting in a single amplitude value for each wavelength. These values are then uploaded to a local buffer in 16 bit words via the data bus

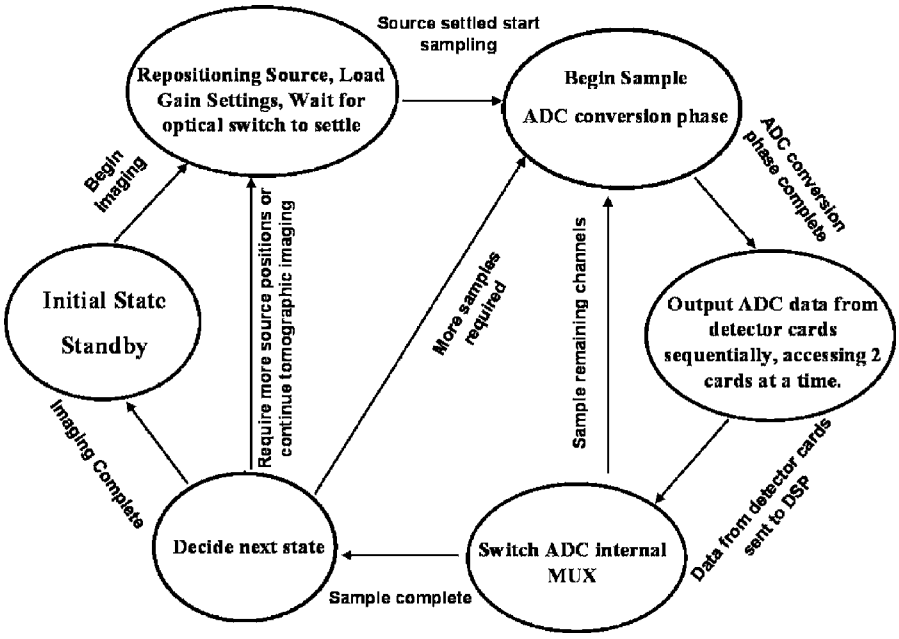

FIG. 8. State machine flow of imaging progression carried out by the CPLD.

where it is retrieved by the data acquisition card and streamlined into the host. The process is repeated for all source locations. To expedite the data flow and maximize the frame rate, the settling time for the subsequent source position is carried out in parallel with the lock-in computation of the current position.

2. CPLD

Duties performed by the CPLD include regulating the sampling frequency, directing the conversion process of the ADC's, switching the internal ADC address bit, and multiplexing the parallel data into a serial stream. While the CPLD also performs some timing control over the gain-bit distribution, its main role is in organizing the sampling process. The complexity is appreciated by the realization that our objective is to multiplex 32 channels, 150 samples/channel, and 16 bits/sample into a single serial port in 2 ms. The state machine associated with the imaging progression is illustrated in Fig. 8. Immediately upon entering the imaging state machine, the address of the first source position is sent to the optical switch and the CPLD waits for the 5 ms settling time pulse from the DSP timer. When the electronics have settled, the CPLD initiates the conversion process for all eight analog-to-digital converters simultaneously. Since each ADC contains two on-chip track-and-hold successive approximation converters, two of their four analog inputs can be digitized concurrently. Therefore, in effect, 16 channels are sampled in parallel. The graphic in Fig. 9 provides greater conceptual acuity to the sampling and multiplexing organization of the data transfer. Upon completion of the conversion process, the data is acquired in a time-division multiplexed fashion and transferred to the DSP along one of its serial ports. Each serial port has two distinct data lines enabling the digitized samples from two separate converters to be retrieved in parallel. After the samples are securely stored in the digital processor's memory, the internal address of all ADC's are switched allowing the remaining channels to be digitized. By dividing down the 30 MHz master clock, a sampling frequency of 75 kHz is maintained per channel. The timing scheme for the continuous data acquisition process is shown in Fig. 10. We can see that the imaging period is strictly governed by the settling time of the optical switch and analog electronics and by the sampling constraints. Therefore, 7 ms is the lower limit in the data acquisition collection speed per source. By ensuring that all DSP processes and PC transfers occur within this time window, we have maximized our realizable frame rate.

3. Digital DAQ card

Operational control of our imaging system is managed by a dedicated host computer that is administered by the

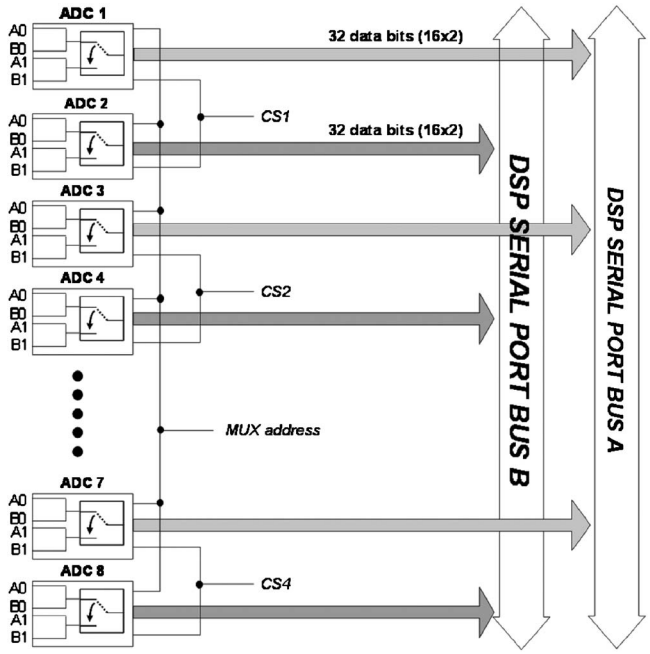

FIG. 9. Illustration of sample read process. Two ADC's are accessed simultaneously, each direct two detector channels worth of data (32 bits) over separate data port lines.

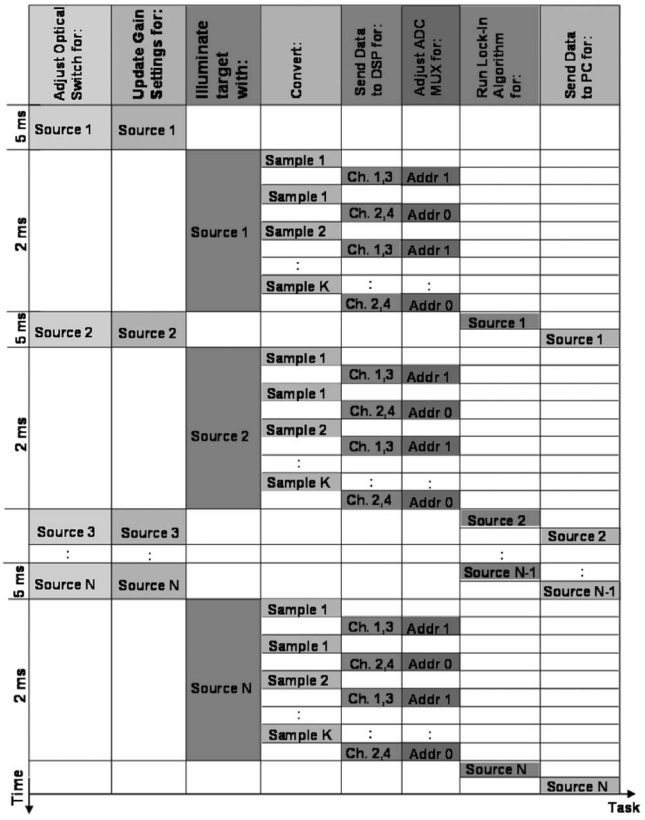

FIG. 10. The timing diagram during the data acquisition sequence for each source position. Most of the time constraints are caused by the settling time of the optical switch and analog electronics. The lock in and data transfer for source N occurs in parallel with the settling time of source $N+1$.

user. The National Instruments PCI-6533 high-speed, 32 bit, parallel, digital I/O interface is used to establish a link network for transferring data and maintaining system control. Its platform can support single-point I/O and pattern I/O over a wide range of hardware-based handshaking protocols providing a stable and robust communication link.

The PCI-6533 contains four digital ports, each port comprised of 8 bits and individually configurable. Two ports are designated as a bidirectional data bus, one port is used for glue-logic control lines, and the fourth port is unused. The 16 bit data bus serves to upload the gain-bit information from the operating software to the DSP and to receive the acquired measurement data as the system is operating in imaging mode. During gain-bit transfers, the data acquisition (DAQ) card acts as master device using a pattern I/O protocol with an internally generated request (REQ) signal to latch a single data word onto an external register. The frequency of the REQ pulse is programable and, since that these operations are not time critical, is set to 65 kHz in the DAQ driver. For each request signal the DSP which is operating in slave-master mode pulls the data off the latch. In this way, the DAQ card may hold back or pace the much faster DSP until the data is valid. However, when accepting imaging data, the DSP acts as master device and dumps the processed data into a buffer in preparation for the next packet of incoming samples. The DAQ card is triggered by a flag on the buffer and the data are collected with a synchronous burst-transfer

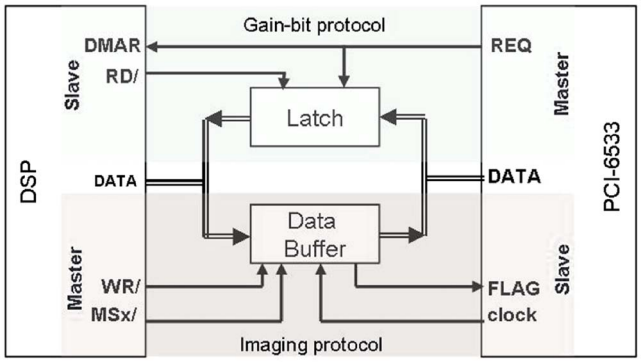

FIG. 11. (Color online) Interconnection between digital DAQ board and DSP timing board. The upper region shows the signaling for gain-bit transfers while the lower region displays the imaging protocol.

timing scheme clocked at ~100 kHz until the buffer is empty. Figure 11 shows the general interconnection schematic between the two devices.

E. Software control and user interface

The software interface with which the operator interacts is developed in LABVIEW (National Instruments) and comprises the instrument configuration, data display and monitoring, and signal postprocessing. A more fundamental software level, which is transparent to the user, coordinates the timing of the peripheral handshaking protocols, data transfers, and data storage. The goal of this software platform is to provide a comprehensive control center that not only manages all user-related tasks associated with imaging but also affords extensive signal viewing and postprocessing capabilities.

The control panel is organized into multiple pages separated by function. Each page allows the user to perform specific tasks such as experimental setup, gain calibration, data acquisition control, and post processing. Figure 12 shows a screen shot of the graphical user interface used to configure the detector gains. A slider is designated for each detector channel and sets the gain for the source position selected by the dial. Since the instrument supports 1024 independent measurements (16 sources, 32 detectors, two wavelengths), manual determination of the gain settings would take upward of 30 min for each experiment. Obviously, in order for the instrument to afford any practical service this restriction becomes unacceptable. As a resolution, we have implemented an automated system calibration routine that scans the target at all possible gain combinations once the fiber optics, measurement probe, and initial scan conditions are fixed in place. The program then evaluates the optimal setting for every source-detector pair by comparing the values of all wavelengths and finding the gain setting in which the signals are above a user-specified threshold and below saturation. The entire automated function is carried out in less than 3 seconds. Signal levels can be verified by scrolling through all wavelengths. Any optode combination in which an appropriate gain setting was not found automatically is tabulated in a chart that directs the user to the exact source/detector/

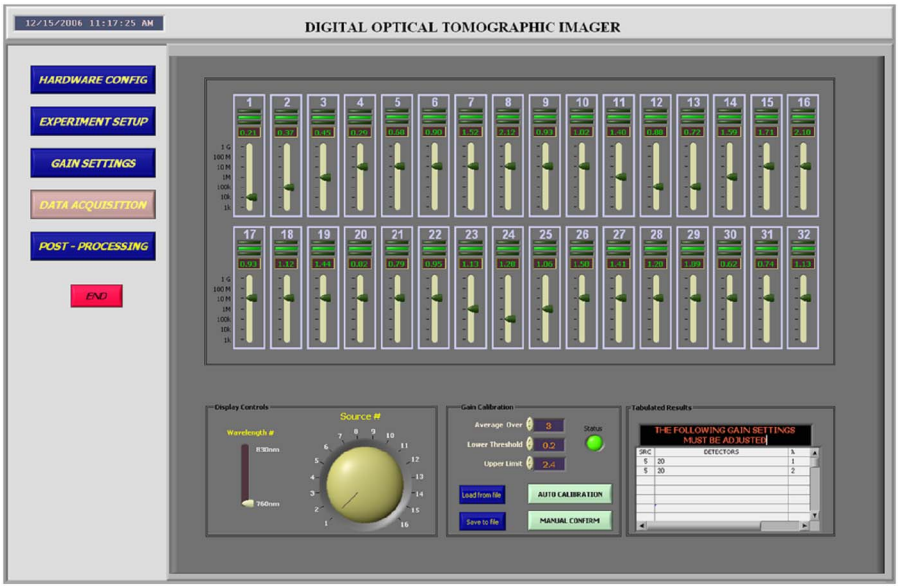

FIG. 12. (Color online) Gain control panel. This interface is used to set, confirm, and test the gain settings for all source-detector pairs. An automatic calibration is available to determine the optimal gain settings in less than 3 s.

wavelength combination that requires a manual adjustment. As part of the calibration process, the gain bits are automatically uploaded and distributed.

The instrument is ready to begin imaging after the system calibration is complete. A designated tab on the user interface manages the data acquisition as shown in Fig. 13. This software package offers versatile data-viewing capabilities allowing real-time monitoring of the imaging progress and alerts the user to any unusual activity. In its general operation, incoming data is plotted on a two dimensional wave form chart where the frame number is represented on the *x*-axis and the amplitude on the *y*-axis. Specific functional characteristics, such as collective temporal changes or precise signal fluctuations, for example, may be enhanced by modifying the display options. Another feature permits reducing common-source noise from all the channels by normalizing against a reference channel. The raw data set for each wavelength is automatically saved to a designated file to be used for image reconstructions.

A graphical data analysis program is an additional tool that is provided in the operating software. It allows the viewer to process, filter, analyze, and display any saved experiment file. In this manner, one can quickly examine an experiment, evaluate the quality of the data, and determine if any portions need to be repeated. It also assists in identifying possible source/detector combinations that should be excluded from the image reconstruction. Data output from this program is in a format that is suitable for running a reconstruction algorithm.

III. SYSTEM PERFORMANCE EVALUATION

To assess the operative effectiveness of the instrument, we have evaluated a range of performance characteristics and verified system specifications. In this way, we were able to determine if our functional objectives were realized through our initial design hypothesis and its implementation.

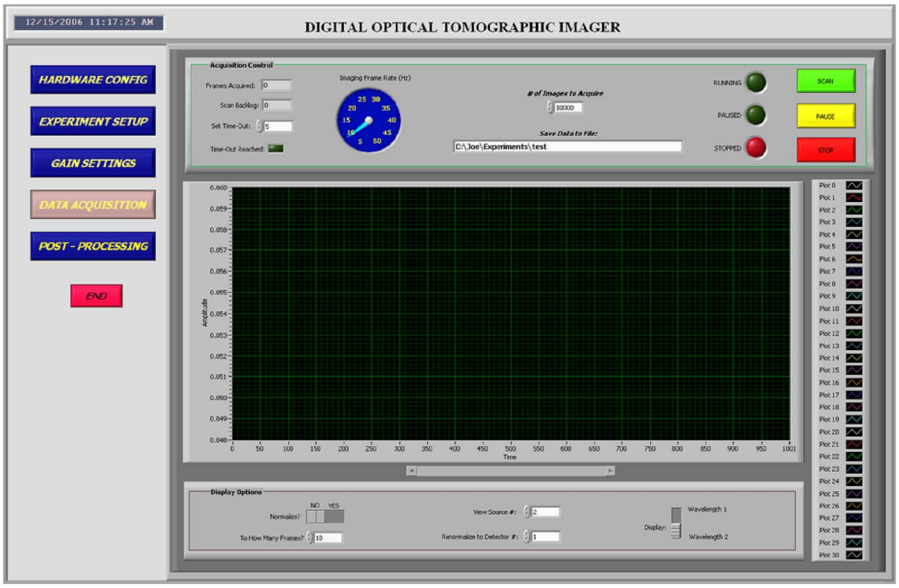

FIG. 13. (Color online) Image acquisition control panel. This screen is used to manage the imaging process and monitor incoming data. Numerous display options are available and configurable on the fly.

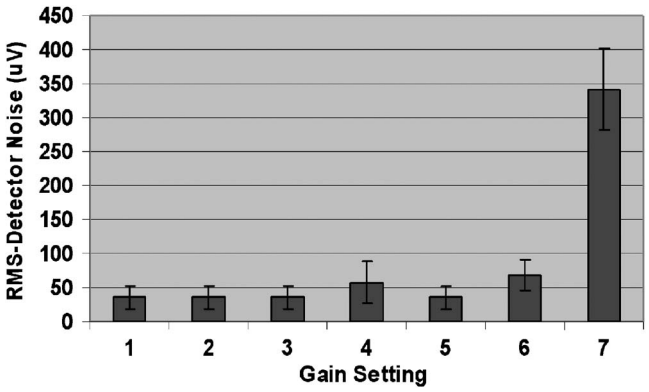

FIG. 14. Mean rms dark-measurement readings for each gain setting.

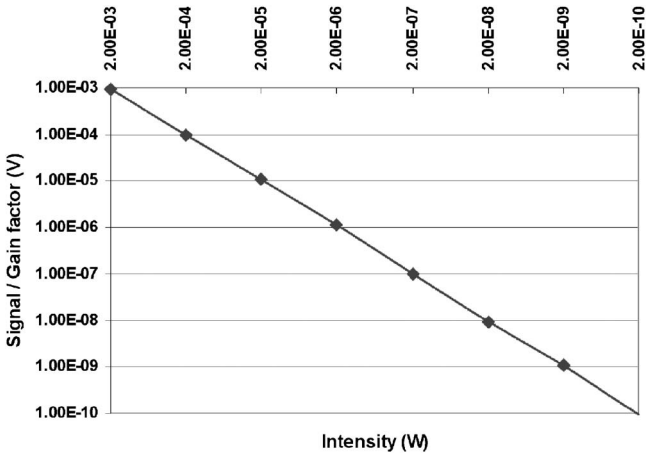

FIG. 15. Linearity curve of instrument detection over measureable dynamic range.

The first parameter to be characterized was the dark signal that is produced when zero light is incident on the photodiode, whose evaluation establishes the noise floor of the detection electronics. Since the lock-in removes the dc component of the original signals and is performed in the digital domain, which themselves do not produce any offset, we expect any residual offset value to be null. Figure 14 displays the root mean square (rms) voltage of the dark readings as a function of channel gain. Each bar represents the mean value of all detector channels in the instrument and the error bars denote the standard deviation. Not surprisingly, this illustration demonstrates that the noise level increases in the instances of highest PGA gain especially at maximum amplification. Such an effect can be assumed because the PGA magnifies any noise produced by the transimpedance stage completely as opposed to increasing the TIA gain which only decreases the signal-to-noise ratio (SNR) by the noise square root. Even in this worst case scenario though, the mean dark voltage is only ~0.35 mV with a standard deviation of about 0.05 mV. In all other settings the mean voltage is even lower at ~0.04 mV.

Using the quantities from these dark measurements, we are able to evaluate the detector sensitivity. Specifically, the noise equivalent power (NEP) is computed for a SNR of unity. Taking the mean plus standard deviation of the maximum recorded dark measurement at the highest detector amplification, we calculate a noise equivalent power of about 2.2 pW peak-to-peak or ~1.6 pW rms. At the opposite end, signal saturation within the range of detection linearity defines the upper signal limit. Saturation occurs when a signal amplitude greater than 2.5 V peal-to-peak is received at the ADC for the lowest gain setting. The corresponding photodiode current is therefore ~2.5 mA. The ratio of signal saturation to the NEP characterizes the system dynamic range and was established to be on the order of 190 dB.

The next task was to characterize the linearity of the system and required a two step process. First, a single optical source is incident on a small diffusive target while the exiting beam was measured by a calibrated power meter (Industrial Fiber Optics, model IF-PM). This value was then compared to the instruments' detected reading of this same photon flux, compensating for the applied amplification. Neutral density filters were used to vary the incident flux levels as the measurements were repeated. It should be noted that the resolution limit of the photometer is on the order of nanowatts and does not allow evaluation at the lower-end range of energies. The results from this study are shown in Fig. 15, which demonstrates that a linear relationship is in fact maintained over the measurable dynamic range of the detectors.

System precision measurements were taken on a homogeneous static phantom over a 5 min time period (~2500 images) for different gain settings. The results of these studies are shown in Fig. 16. The columns represent the mean coefficient of variation (CV) among all channels at the stated gain, where gain of 1 is the lowest gain setting and gain of 7 is the highest. The error bars signify the standard deviation of the calculated CV's. Signal variability is exceptionally low for gain stages of 1, 2, 3, and 5, with CV's ranging between 0.02% and 0.06%. At these levels, the detector noise is extremely low and the dominant noise contributors are the laser source and coupling inefficiencies. At gain of 4, the high PGA setting results in greater noise amplification as we see the CV slightly increase to about 0.12%. The CV's for gains of 6 and 7 are progressively larger due to greater detector noise at the highest gain values. However, if we calculate the corresponding signal to noise ratio as

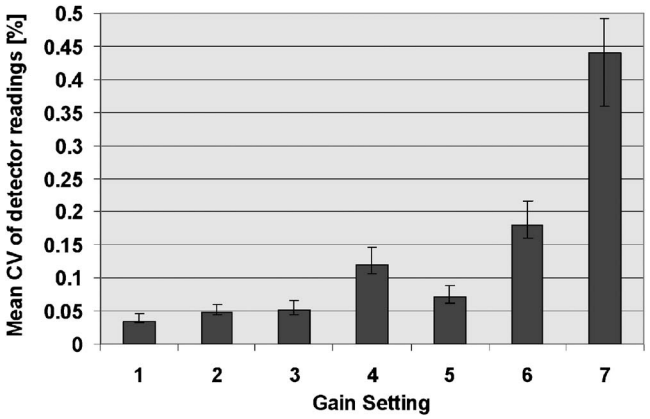

FIG. 16. Mean CV of detector channels as a function of gain setting.

$$\mathrm{SNR} = 20 \log_{10} \frac{m_{s,d}}{\sigma_{s,d}}, \tag{16}$$

where the noise level $\sigma_{s,d}$ is defined as the standard deviation around measurement vector $m_{s,d}$ taken at source s and detector d, we observe that even at the highest mean CV of just under 0.5%, the corresponding signal to noise ratio is approximately 48 dB which is still remarkably high.

Long term stability was measured by continuously imaging a static intralipid phantom for over 40 min (~20 000 continuous measurement frames). All gain settings were calibrated at the appropriate level to closely correlate with a typical experimental setup. In this way, all components that contribute to the overall system drift such as the laser diodes, their driving circuitry and the analog detection electronics may be accurately represented. The collective drift of ±1% over this time period was identified by noting the difference between the initial and final images.

Electrical cross talk between detector channels is a potential concern as interference reduces the signal precision. Since the front-end analog electronics of four separate channels share a single printed circuit board, it is here that cross talk is most likely to occur. Beyond this point and throughout the rest of the system, all signals propagate in the digital domain, which is decidedly more immune to cross talk effects. Furthermore, with active shielding around each high-impedance sensor in conjunction with the physical disconnect of individual boards, crosstalk from one PCB to the next is expected to be orders of magnitude less. Therefore, we only need to determine the cross talk experienced among the four interconnected detectors as that will assume the limiting value. These measurements were conducted by imaging through an absorptive target thereby requiring the use of higher amplification. Each of the four detector channels was sequentially removed from their sensor during the data acquisition, and the signal fluctuations for the remaining channels were noted. To isolate cross talk effects from other system noise, the above procedures were repeated several times and a block averaging was computed on the data set. We have observed that the crosstalk quantity in all source-detector instances is <0.01% of the signal.

Another source of interference is optical cross talk. Optical isolation can be an important parameter because of the very large dynamic range afforded by the detector electronics. As such, it must be demonstrated that light from one channel does not influence the signal of another. Photon leakage can occur in one of two places: either within the optical switch or at the detector enclosure. Within the switch, internal reflections and imperfect couplings can cause stray light to reach the target through the "dark" fiber bundles and is an inherent function of the switch. To assess cross talk at this stage we illuminate a single source position but direct the light away from the target and disable the rest of the switch address positions. We then compare measurements that were performed when the laser sources are on versus when the laser diodes are turned off. Any difference in signal is a direct consequence of internal leakage. We have observed that the optical switch cross talk for any optode combination is <85 dB optical power.

TABLE I. Performance characteristics of digital instrument.

Parameter	Value
Noise equivalent power	~1 pW rms
Dynamic range	~190 dB
Dark noise amplitude	<50 μV (at lowest gain setting) <400 μV (at highest gain setting)
Long term stability	<±1% (over 40 min.)
Interchannel cross talk	<0.01%
Optical cross talk (switch)	<85 dB (power)
Optical cross talk (detection interface)	<95 B (power)
Precision	<0.04%–0.3% depending on signal strength
Temporal response	8.9 Hz (at 16 source positions) 140 Hz (at 1 source position)
Light power to tissue	22 mW at 765 nm, 20 mW at 830 nm

Optical cross talk contained within the detection housing occurs at the fiber-photodiode interface. For this reason, each fiber termination and photodetector is fully encapsulated in individual ferrules and physically separated from other sensors. To quantify this parameter, a comparison was made between signal intensities at a specific channel when light is directed to an alternate detector channel and when that light is removed. In this instance, measurements were made on all channels except the one being illuminated, which maintained the lowest possible gain setting to minimize the electrical cross talk. These comparative measurements yield a photon isolation of <95 dB power.

Finally, we need to quantify the temporal resolution of the imager. It is this parameter that defines what dynamic physiologic process may be accurately extracted and which will become aliased. The speed is dependent on four constraints: the settling time of the optical switch, the settling time of the analog electronics, the dwell time of each source position, and the number of sources used. The settling time for both the switch and circuitry is 5 ms and occur in parallel. An additional 2 ms is required for the data acquisition period. So data is collected at each source every 7 ms. Since the only nonfixed dependency is the number of source positions, it will directly govern the temporal response. Therefore, at a single source position images can be acquired at speeds as high as 140 Hz, while at the full 16 source positions, they are collected at about nine frames per second. Generally, the imaging rate may be calculated as 140 Hz divided by the number of sources in use. A summary of the more important performance characteristics are listed in Table I.

IV. PHANTOM STUDIES

The intent of these experiments is to evaluate the accuracy of the collective instrument performance under regulated conditions. This depends on the quality of the imaging data and the exactness of the reconstruction algorithm. As discussed in the Introduction an important application in dynamic optical tomography is recording instantaneous spatiotemporal changes in optical properties relative to a previ-

ous baseline or mean signal value. This has relevance, for example, in monitoring blood volume, hemodynamics, and blood oxygenation states during functional activation or in response to an external stimulus. We have therefore devised a method for collecting such data types while at the same time providing a means with which to establish system functionality. Some measures of interest include multiple object detectability, quality of reconstructed image, and defining how well the spatial position of a dynamic phantom can be tracked. While many of these parameters are limited by the inherent capabilities of the image reconstruction algorithm, nonetheless the quality of the data set generated by the instrument has a significant impact on the resulting image quality. However, it should be noted that a comprehensive examination of these parameters is beyond the scope of this study.

We approach these tasks by acquiring images on a fixed-geometry probe containing inserted objects that are moved in a predefined manner relative to a predetermined optode configuration. In this manner, the accuracy with which the objects are resolved from the background medium and their position localized with respect to the probe boundaries may be determined.

A. Experimental setup

The measurement probe used was cylindrical in shape and composed of a white Delrin material that measures 3.2 cm in diameter, a wall thickness of 1.0 mm, and 15 cm in length. A translatable ring that slides over the cylinder secures the source and detector fiber bundles. The ring can accommodate up to 24 fibers so we employ 12 sources and 12 detectors arranged in an alternating clockwise configuration for a total of $12\times12=144$ source-detector combinations. Approximately ten complete tomographic data sets were collected per second. A single time frame included the illumination of each of the 12 sources in succession and detection of the transmitted light received through all 12 detectors simultaneously. The background medium consisted of a 1% concentration of intralipid emulsion that filled the volume of the vessel.

The absorption of the intralipid is essentially due to water[62,63] so we introduce an ink suspension to provide an absorptive heterogeneity[64] without having a significant impact on the scattering coefficient.[65] More specifically, a round straw measuring 1.8 mm in diameter filled with a solution that was 0.2% India ink by volume made up the contrasting inclusions. While we did not independently measure the optical properties of the inclusions, the scattering coefficient has been reported[66] as $\mu_s'=10\ \mathrm{cm}^{-1}$ and the absorption coefficients may be extrapolated from documented values[67] to be $\mu_a=0.51\ \mathrm{cm}^{-1}$.

A diagram of the three phantom trials shown in a cross-sectional view is depicted in Fig. 17. In the first study, a single inclusion was manually guided around the circumference of the probe in a clockwise rotation [Figure 17(a)]. The second experiment used the same inclusion but was translated across the diameter of the probe beginning in the "10 o'clock" position and ending in the "5 o'clock" position [Fig. 17(b)]. The final experiment employed two straw inclusions located in the 12 and 6 o'clock positions separated by 20 mm and are rotated into the 3 and 9 o'clock positions, respectively. All measurements are taken relative to a homogeneous intralipid base line.

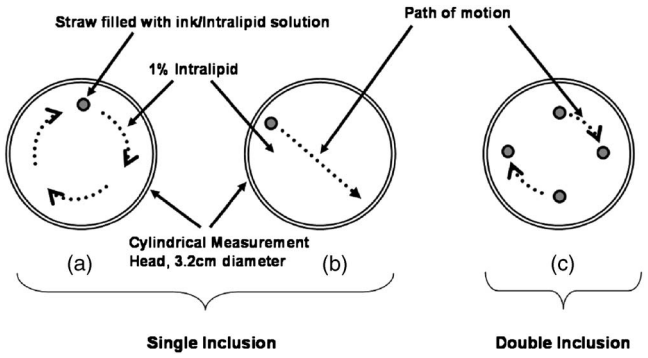

FIG. 17. Experimental setup for phantom experiments shown in cross-sectional view. (a) Single inclusion rotated clockwise around cylindrical vessel, (b) single inclusion translated across vessel, and (c) double inclusion 20 mm apart rotated 90°.

To generate three dimensional images from the collected data, a model-based iterative image reconstruction (MOBIIR) scheme was employed.[68,69] This technique solves the continuous wave diffusion equation for a finite-element discretization over a volume of interest. Based on documented values, our initial guess for the absorption coefficient μ_a and the diffusion coefficient $D=c/3(\mu_a+\mu_s')$ was 0.10 cm^{-1} and 0.924 $\mathrm{cm}^2/\mathrm{ns}$, respectively. Details on the particulars of the algorithm can be found in Ref. 13.

B. Results

A sample time trace of the first phantom experiment is shown in Fig. 18. It represents the 12 detector profiles from source position 1, wavelength $\lambda1=760$ nm, normalized to the homogeneous baseline. As the light-absorbing target moves throughout the vessel, the signal amplitudes seen at the stationary channels continuously change. The recovered images for the first data set is shown in Fig. 19 as the cross-sectional spatial mapping of the localized changes in absorp-

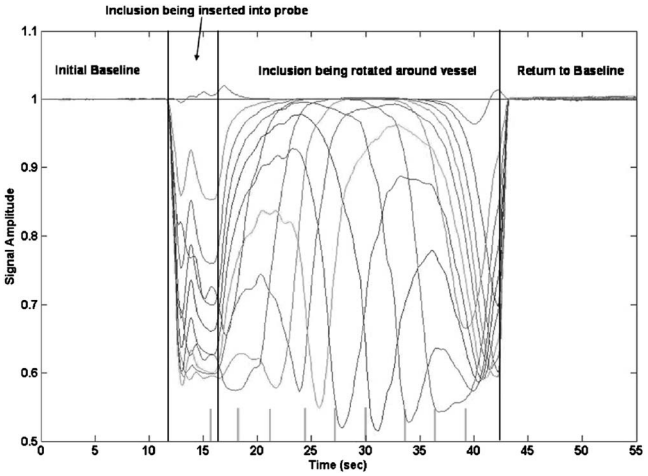

FIG. 18. Time traces of all detectors for a sample source position (src 1) wavelength of 765 nm during the first dynamic phantom experiment. Responsivity of each channel changes as the absorbing target moves.

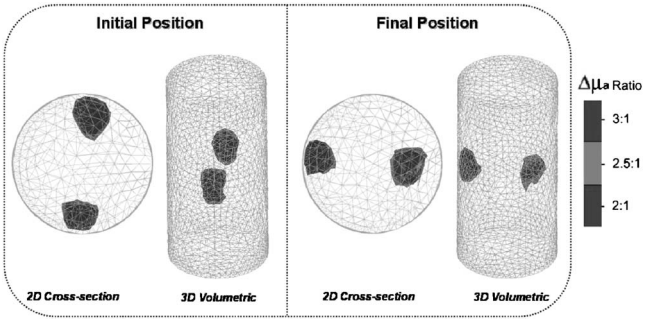

FIG. 21. Reconstruction results (λ=765 nm) from the third and final phantom experiment shown in the three dimensional (3D) volumetric mesh. The left side represents the initial positions of the inclusions and the right side depicts the final positions.

tion $\Delta\mu_a$ progress as a function of time. The initial image corresponds to a time point of 15 s into the experiment when the inclusion has been inserted into the probe. Each subsequent image is captured every 3 s thereafter until a complete 360° rotation has been achieved. From this example we can clearly see that the instrument correctly tracks the trajectory and identifies the location of embedded objects. By enlarging the images, the dimensions of the reconstructed target can be better evaluated and we find that it generally has two distinct diameters: an inner diameter core measuring ~1.9 mm wide with a $\Delta\mu_a$ of 4:1 with respect to the baseline and an outer diameter at ~3.5 mm with a $\Delta\mu_a$ about 3.7 times greater. The inner core closely corresponds with the physical dimensions of the inclusion while the outer diameter results from the spatial resolution limits of the algorithm. Similarly, Fig. 20 shows the reconstructed images of the localized changes in μ_a for the second measurement. Here too we see that the target features and positions are accurately recovered.

Images generated from the third experiment are depicted in Fig. 21. Here we provide the three dimensional rendering of the two inclusions as they are reconstructed within the vessel. For enhanced visualization, the images were captured at two viewpoints: (1) looking down into the cylindrical probe and (2) angled upright. Again, we observe correct characterization of the targets and note that the center-to-center distance between the objects was measured at ~19.5 mm, which very closely matches their physical separation. However, we find that the size of the inclusions depicted in the $\Delta\mu_a$ distribution is considerably overestimated. This is likely due to the resolution limits dictated by the grid size and the inherent limitations of the reconstruction code.

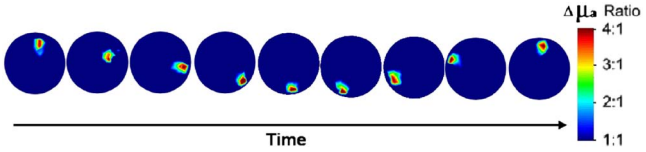

FIG. 19. (Color online) Cross-sectional reconstruction results (λ=765 nm) from the second phantom experiment. Images taken from the time of the inclusion is immersed and every 3 s thereafter until the translation across the probe is complete. The recovered object also seems to follow the object pathway.

TABLE II. Comparison chart between first generation analog and second generation digital optical tomography systems.

	DYNOT	Digital imager
Mode of operation	CW	CW
No. of wavelengths	1–4	1–4
No. of sources/detectors	25/32	16/32
Dynamic range	180 dB	190 dB
Sensitivity (NEP)	10 pW	1 pW
Precision (% CV) (for identical gain settings)	0.2%–30% depending on signal strength	0.05%–0.5% depending on signal strength
Data rate (Hz)[a]	2160–8640	4608–18432
Acquisition time	0.37 s	0.11 s
Dark noise	~1–10 mV	20–400 μV
Instrument size[b]	~6200 in.^{3}	~2900 in.^{3}

[a]Corresponds to a complete imaging frame.
[b]Takes into account components only, not enclosing cart.

V. DISCUSSION

A. Comparison to existing analog system

The recent interest in developing pragmatic measurement systems for optical tomography can be appreciated by the number of such articles published in the literature. It is therefore instructive to not only characterize the functionality of our newly designed imager but to also put its performance in perspective of other reported systems. A detailed comparison of different optical instrumentations spanning the three different measurement techniques (time domain, frequency domain, and continuous wave) was presented by Schmitz *et al.*[25] in association with the introduction of their DYNOT system. Since the digital instrument outlined in this article is a second generation development of DYNOT, we will offer a direct comparison against that system only and the interested reader is referred to the cited paper for a more comprehensive comparative assessment.

Table II illustrates some general performance differences between the two instruments. Both instruments operate in the continuous wave domain, accept up to four independent wavelengths, and detect 32 parallel channels simultaneously. However, a direct comparison of the functional parameters confirms that the implementation of digital acquisition and detection techniques leads to improvements most notably in the detection sensitivity, precision, dark noise, and data acquisition speed. For many channels of the DYNOT system the detector precision is <1% for all channels; however, at higher gain settings their SNR falls off dramatically with

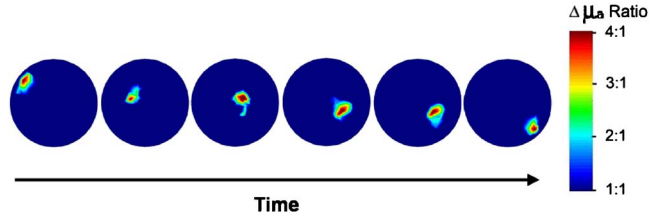

FIG. 20. (Color online) Reconstruction results (λ=765 nm) from the first phantom experiment. Images taken from the time of the inclusion is immersed and every 3 s thereafter until a complete rotation is formed. The recovered object is observed rotating in a counterclockwise direction.

reported CV's as high as 50%. It is also valuable to point out that the physical size of the digital imager is significantly smaller than DYNOT and can be reduced further yet by compacting the PCB layout. This technology encourages the application of a small lightweight imaging solution that can be easily transported and set up at a patient's bedside.

There are also some practical benefits realized by the layout and structure of this new instrument. Firstly, the modular design of our detection electronics, particularly the gain-bit circuitry, has made adding detector channels an effortless task unlike the analog system which uses a separate timing board to manage the gain-bit control. Secondly, our quadrature processing algorithm eliminates the need for phase-shifter boards. Finally, unlike DYNOT whose optical in-coupling and focusing mechanism is sensitive to motion and vibration making transport difficult, the optics in our system were designed to be portable making them impervious to the typical vibrations associated with movement.

B. Summary

This article presented a new dynamic optical tomography imaging system, which is the first to employ digital signal processing and acquisition techniques. We outlined design considerations and engineering issues concerning the realization of such a system. Specifically, we use a high performance DSP to execute digital lock-in detection algorithms on received signals and direct data flow throughout the instrument and to command system-level management between other peripheral devices. Performing the lock-in detection through software as opposed to analog circuitry increases signal integrity, provides greater functionality, offers extended flexibility and reduces the system cost and size. Furthermore, we have shown that by incorporating quadrature phase sensitive detection, we eliminate the need for individual phase shifters, a significant complexity in multichannel sampled devices. Timing issues are precisely orchestrated through rigorous handshaking protocols between the CPLD, DSP, and data acquisition card. It is because the system operations are so efficiently streamlined that allow for images to be acquired at rates of up to 140 Hz for 32 detector channels. Quantification and analysis of instrument performance demonstrates that making use of precision circuitry in a digital detection environment greatly enhances the system functionality. Initial experiments on tissue phantoms show that the instrument correctly tracks the spatial and temporal response of inclusions. A direct comparison with a first generation analog system shows that we have achieved significant improvements in functional performance with this new design.

ACKNOWLEDGMENTS

This work was supported in part by funds from the National Institutes of Arthritis and Musculoskeletal and Skin Diseases (NIAMS Grant 2RO1 AR46255), which is part of the National Institutes of Health (NIH). Furthermore, we would like to thank Yang Li for his contributions to the LABVIEW and microcontroller programing, Chris Fong for debugging the illumination layout and running the image reconstruction algorithms for the phantom-measurement data, and Randall Barbour for making his resources available as needed.

[1] B. Chance, R. R. Alfano, B. J. Tromberg, M. Tamura, and E. M. Sevick-Muraca, Proc. SPIE **6434** (2007).
[2] B. Chance, R. R. Alfano, B. J. Tromberg, M. Tamura, and E. M. Sevick-Muraca, Proc. SPIE **4250** (2001).
[3] B. Chance, R. R. Alfano, and B. J. Tromberg, Proc. SPIE **4955** (2003).
[4] B. Chance and R. R. Alfano, Proc. SPIE **2389** (1995).
[5] G. Müller *et al.*, *SPIE Institutes for Advanced Optical Technologies Series*, (SPIE, Bellingham, 1993), Vol. IS11.
[6] A. J. Welch and M. J. C. van Gemert, *Optical-Thermal Response of Laser-Irradiated Tissue* (Plenum, New York, 1995).
[7] R. L. Barbour, H. L. Graber, Y. Pei, S. Zhong, and C. H. Schmitz, J. Opt. Soc. Am. A **18**, 3018 (2001).
[8] S. G. Diamond, T. J. Huppert, V. Kolehmainen, M. A. Franceschini, J. P. Kaipio, S. R. Arridge, and D. A. Boas, Neuroimage **30**, 88 (2006).
[9] A. Y. Bluestone, G. Abdoulaev, C. Schmitz, R. L. Barbour, and A. H. Hielscher, Opt. Express **9**, 272 (2001).
[10] E. Ohmae *et al.*, Neuroimage **29**, 697 (2006).
[11] X. F. Zhang, V. Y. Toronov, and A. G. Webb, Opt. Express **13**, 5513 (2005).
[12] J. Selb, M. A. Franceschini, A. G. Sorensen, and D. A. Boas, J. Biomed. Opt. **10**, Art. No. 011013.
[13] A. Y. Bluestone, M. Stewart, J. Lasker, G. S. Abdoulaev, and A. H. Hielscher, J. Biomed. Opt. **9**, 1046 (2004).
[14] J. C. Hebden *et al.*, Phys. Med. Biol. **49**, 1117 (2004).
[15] A. P. Gibson, J. C. Hebden, and S. R. Arridge, Phys. Med. Biol. **50**, R01 (2005).
[16] J. C. Hebden, S. R. Arridge, and D. T. Deply, Phys. Med. Biol. **42**, 825 (1997).
[17] S. R. Arridge and J. C. Hebden, Phys. Med. Biol. **45**, 841 (1997).
[18] A. H. Hielscher, A. Y. Bluestone, G. S. Abdoulaev, A. D. Klose, J. Lasker, M. Stewart, U. Netz, and J. Beuthan, Dis. Markers **18**, 313 (2002).
[19] C. H. Schmitz *et al.*, Appl. Opt. **39**, 6466 (2000).
[20] T. Vaithianathan, D. C. Tullis, N. Everdell, T. Leung, A. Gibson, J. Meek, and D. T. Deply, Rev. Sci. Instrum. **75**, 3276 (2004).
[21] S. Zhao, M. A. O'Leary, S. Nioka, and B. Chance, Proc. SPIE **2389**, 809 (1995).
[22] Q. Luo, S. Nioka, and B. Chance, Proc. SPIE **2979**, 84 (1997).
[23] S. B. Colak, M. B. van der Mark, G. W.'t Hooft, J. H. Hoogenraad, E. S. van der Linden, and F. A. Kuijpers, IEEE J. Sel. Top. Quantum Electron. **5**, 1143 (1999).
[24] M. Niwayama, K. Yamamoto, D. Kohata, K. Hirai, N. Kudo, T. Hamaoka, R. Kime, and T. Katsumura, IEICE Trans. Inf. Syst. **E85-B**, 115 (2002).
[25] C. H. Schmitz, M. Löcker, J. M. Lasker, A. H. Hielscher, and R. L. Barbour, Rev. Sci. Instrum. **73**, 429 (2002).
[26] Y. Yamashita, A. Maki, and H. Koizumi, J. Biomed. Opt. **4**, 414 (1999).
[27] A. M. Siegel, J. A. Marota, and D. A. Boas, Opt. Express **4**, 287 (1999).
[28] About Lock-In Amplifiers (www.thinkSRS.com) Stanford research Systems, Application Note No. 3.
[29] T. I. Oh, J. W. Lee, K. S. Kim, J. S. Lee, and E. J. Wu, Proceedings of the 25th IEEE EMBS Annual International Conference, 17 September 2003.
[30] A. Hartov, R. A. Mazzarese, F. R. Reiss, T. E. Kerner, K. S. Osterman, D. B. Williams, and K. D. Paulsen, IEEE Trans. Biomed. Eng. **47**, 49 (2000).
[31] A. Albertini and W. Kleeman, Meas. Sci. Technol. **8**, 666 (1997).
[32] S. Cova, A. Longoni, and I. Freitas, Rev. Sci. Instrum. **50**, 296 (1979).
[33] R. Alonso, F. Villuendas, J. Borja, L. A. Barragan, and I. Salinas, Meas. Sci. Technol. **14**, 551 (2003).
[34] S. Fantini, E. L. Heffer, V. E. Pera, A. Sassaroli, and N. Liu, Technol. Cancer Res. Treat. **4**, 471 (2005).
[35] S. Srinivasan *et al.*, Technol. Cancer Res. Treat. **4**, 513 (2005).
[36] L. Spinelli, A. Torricelli, A. Pifferi, P. Taroni, G. Danesini, and R. Cubeddu, Phys. Med. Biol. **50**, 2489 (2005).
[37] S. K. Mitra, *Digital Signal Processing—A Computer Based Approach*, 2nd ed. (McGraw-Hill, New York, 2001).
[38] A. Cova, A. Langoni, and I. Freitas, Rev. Sci. Instrum. **50**, 296 (1979).
[39] P. A. Probst and B. Collet, Rev. Sci. Instrum. **56**, 466 (1985).
[40] F. DeRosa, Rev. Sci. Instrum. **57**, 1693 (1986).
[41] E. Morris and H. Johnston, Rev. Sci. Instrum. **39**, 620 (1968).
[42] G. D. Renkes, L. R. Thorne, and W. D. Gwinn, Rev. Sci. Instrum. **49**, 994 (1976).

[43] S. Carrato, G. Paolucci, R. Tommsini, and R. Rosei, Rev. Sci. Instrum. **60**, 2257 (1989).
[44] F. Barone, E. Calloni, L. DiFiore, A. Grado, L. Milano, and G. Russo, Rev. Sci. Instrum. **66**, 3697 (1995).
[45] S. W. Smith, *The Scientist and Engineer's Guide to Digital Signal Processing*, 2nd ed. (California Technical Publishing, San Diego, CA, 1999).
[46] L. A. Barragan, J. I. Artigas, R. Alonso, and F. Villuendas, Rev. Sci. Instrum. **72**, 247 (2001).
[47] S. G. Castillo and K. B. Ozanyan, Rev. Sci. Instrum. **76**, 095109 (2005).
[48] A. Restelli, R. Abbiati, and A. Geraci, Rev. Sci. Instrum. **76**, (2005).
[49] J. Linn, Proceedings of the Fifth International Symposium on Antonomous Decentralized Systems, 2001, p. 299.
[50] "A Technical Tutorial on Digital Signal Synthesis," Analog Devices Inc. (1999).
[51] W. Kester, Analog devices, MT-001, Rev.0 (2005).
[52] J. Graeme, *Photodiode Amplifiers: Op Amp Solutions* (McGraw-Hill, New York, 1996).
[53] W. Kester, *Analog Devices Technical Reference Books* (Analog Devices, Norwood, MA, 1999).
[54] B. Michel, L. Novotny, and U. Durig, Ultramicroscopy **42–44**, 1647 (1992).
[55] H. Nyquist, AIEE Trans. **47**, 617 (1928).
[56] C. E. Shannon, Proc. IRE **37**, 10 (1949).
[57] J. M. Masciotti, J. M. Lasker, and A. H. Hielscher, IEEE Trans. Instrum. Meas. (accepted for publication).
[58] D. R. Whlte and J. F. Clare, Meas. Sci. Technol. **3**, 1 (1992).
[59] O. Vaino, IEEE Trans. Instrum. Meas. **48**, 1100 (1999).
[60] "Delta Sigma A/D Conversion Technique Overview," *Application Note AN 10*, Crystal Semiconductor Corporation, TX (1989).
[61] J. DiBartolomeo and D. Cecic, IEEE Instrumentation & Measurement Society Meeting, Toronto Chapter, October 2003.
[62] B. C. Wilson, M. S. Patterson, and B. W. Pogue, Proc. SPIE **1892**, 132 (1993).
[63] B. W. Pogue, M. S. Patterson, H. Jiang, and K. D. Paulsen, Phys. Med. Biol. **40**, 1709 (1995).
[64] R. Cubeddu, A. Pifferi, P. Taroni, A. Torricelli, and G. Valentini, Phys. Med. Biol. **42**, 1971 (1997).
[65] S. J. Madsen, M. S. Patterson, and B. C. Wilson, Phys. Med. Biol. **37**, 985 (1992).
[66] H. J. van Staveren, C. J. M. Moes, J. van Marle, S. A. Prahl, and M. J. C. van Gemert, Appl. Opt. **30**, 4507 (1991).
[67] M. Gurfinkel, T. Pan, and E. M. Sevick-Muraca, J. Biomed. Opt. **9**, 1336 (2004).
[68] A. H. Hielscher, A. D. Klose, and K. M. Hanson, IEEE Trans. Med. Imaging **18**, 262 (1999).
[69] A. D. Klose and A. H. Hielscher, Med. Phys. **26**, 1698 (1999).